

Stellar halos of bright central galaxies II

Scaling relations, colours and metallicity evolution with redshift

Emanuele Contini¹ *, Marilena Spavone², Rossella Ragusa², Enrichetta Iodice², and Sukyoung K. Yi¹

¹ Department of Astronomy and Yonsei University Observatory, Yonsei University, 50 Yonsei-ro, Seodaemun-gu, Seoul 03722, Republic of Korea

² INAF Osservatorio Astronomico di Capodimonte, Salita Moiariello 16, 80131 Napoli, Italy

March 11, 2026

ABSTRACT

Aims. We investigate the formation and evolution of stellar halos (SHs) around bright central galaxies (BCGs), focusing on their scaling relations, colours, and metallicities across cosmic time, and we compare model predictions with ultra-deep imaging data.

Methods. We use the semi-analytic model FEGA25, applied to merger trees from high-resolution dark matter simulations, including an updated treatment of intracluster light (ICL) formation. SHs are defined as the stellar component within a physically motivated transition radius, linked to the structural properties of the host halo. Predictions are compared with observations from the VST Early-type GALaxy Survey (VEGAS) and Fornax Deep Survey (FDS).

Results. The SH mass correlates well with both BCG and ICL masses, with tighter scatter in the SH–ICL relation. The transition radius peaks at 30–40 kpc nearly independent of redshift in the model predictions, but can reach ~ 400 kpc in the most massive halos, after $z = 0.5$. SHs and ICL show nearly identical colour distributions at all epochs, both reddening toward $z = 0$. At $z = 2$, SHs and the ICL are ~ 0.4 dex more metal-poor than BCGs, but the gap shrinks to ~ 0.1 dex by the present time. Observed colours are consistent with model predictions, while observed metallicities are lower, suggesting a larger contribution from disrupted dwarfs.

Conclusions. SHs emerge as transition regions between BCGs and the ICL, dynamically and chemically coupled to both. Their properties depend on halo concentration, ICL formation efficiency, and the progenitor mass spectrum. Upcoming wide-field photometric and spectroscopic surveys (e.g. LSST, WEAVE, 4MOST) will provide crucial tests by mapping structure, metallicity, and kinematics in large galaxy samples.

Key words. Galaxies: clusters – Galaxies: evolution

1. Introduction

Stellar halos (SHs) are diffuse, low surface-brightness (LSB) stellar envelopes that surround galaxies and preserve a fossil record of past accretion events and early phases of in-situ star formation (Bullock & Johnston 2005; Cooper et al. 2010). Their study has become a cornerstone for understanding the hierarchical build-up of galaxies within the Λ CDM framework, since halo stars are long-lived and retain chemical and dynamical imprints of their progenitors (Helmi 2008; Font et al. 2011; Duc et al. 2015; Iodice et al. 2016; Lane et al. 2022; Beltrand et al. 2024).

Photometric surveys of resolved red-giant branch (RGB) stars in nearby galaxies have shown that colours can serve as robust proxies for metallicity, under reasonable assumptions about stellar ages (Monachesi et al. 2016; Harmsen et al. 2017). These surveys reveal a remarkable diversity: while some halos display strong negative colour and metallicity gradients (bluer, more metal-poor populations at larger radii), others show almost flat profiles over tens of kiloparsecs (Mouhcine et al. 2005; Ibata et al. 2014). In the Milky Way, spectroscopic surveys have established a clear dichotomy between the inner halo, relatively metal-rich, and the outer halo, more metal-poor, consistent with a two-component formation scenario (Carollo et al. 2007; Beers et al. 2012; Deason et al. 2014; Helmi et al. 2018). Similarly, M31 exhibits a pronounced metallicity gradient extending to

large radii, suggesting that its halo has been significantly shaped by the accretion of relatively massive satellites (Kalirai et al. 2006; Gilbert et al. 2014).

A key emerging result is that SH metallicities correlate with host galaxy stellar mass or luminosity: more massive galaxies tend to host more metal-rich halos, a relation consistent with expectations from the mass–metallicity relation of dwarf satellites (Mouhcine et al. 2005; Harmsen et al. 2017; D’Souza & Bell 2018). However, there is large halo-to-halo scatter, reflecting the stochasticity of hierarchical assembly and the diversity of accretion histories (Merritt et al. 2016; Amorisco 2017). Chemical abundance ratios, particularly $[\alpha/\text{Fe}]$, provide further constraints: high $[\alpha/\text{Fe}]$ ratios trace rapid star formation in massive progenitors or in-situ components, while lower values indicate extended star formation in low-mass dwarfs (Venn et al. 2004; Deason et al. 2016).

Recently, ultra-deep wide-field photometric surveys have extended SH studies to a larger variety of environments, including galaxy groups and clusters. The VST Early-type GALaxy Survey (VEGAS) survey has revealed extended halos, tidal features, and intracluster light (ICL) in several nearby systems (Capaccioli et al. 2015; Iodice et al. 2017, 2019; Spavone et al. 2017, 2018, 2020, 2021, 2022, 2024; Ragusa et al. 2023). These studies highlight the strong connection between the outer envelopes of massive early-type galaxies (ETGs) and their accretion histories, with signatures of past mergers, stripping and disruption events.

* e-mail: emanuele.contini82@gmail.com, yi@yonsei.ac.kr

Such results complement stellar population studies in the Local Group, extending SH science to a statistical sample of galaxies in diverse environments.

Theoretical models and cosmological simulations have been instrumental in interpreting these observations. Early semianalytic and particle-tagging models highlighted the role of a few dominant progenitors in building up halos (Bullock & Johnston 2005; Cooper et al. 2010). More recent hydrodynamical simulations, such as AURIGA (Grand et al. 2017), FIRE (Hopkins et al. 2014), and IllustrisTNG (Nelson et al. 2018), demonstrate that both accreted and in-situ components are important: in-situ stars are typically more metal-rich and centrally concentrated, producing steeper gradients, whereas accreted halos are flatter unless shaped by the disruption of massive satellites (Font et al. 2011; Pillepich et al. 2018; Monachesi et al. 2019; Elias et al. 2020). In summary, studies of SH colours and metallicities reveal a complex and diverse picture. Observations point to correlations with host mass and stochastic variations tied to accretion history, while simulations stress the interplay between in-situ star formation and accreted material (e.g., Cooper et al. 2015; Wright et al. 2024). Future wide-field imaging surveys and spectroscopic campaigns—such as LSST (Ivezić et al. 2019), WEAVE (Jin et al. 2024), and 4MOST (de Jong et al. 2019)—will expand halo samples to statistically significant sizes, enabling robust comparisons with cosmological models and yielding new insights into galaxy formation and evolution (Cooper et al. 2011; Helmi 2020; Spavone et al. 2022).

Recent simulation suites have substantially expanded both statistics and physical realism for SH studies. The augmented AURIGA Project adds 40 new Milky Way–mass zooms (plus 26 dwarf-mass systems) at fixed physics, enabling stronger constraints on halo-to-halo scatter in ex-situ fractions, metallicity gradients, and their connection to merger histories (Grand et al. 2017). Within AURIGA, new analyses connect the presence of strongly radially anisotropic debris and steep negative $[\text{Fe}/\text{H}]$ gradients to the dominance of one or a few massive accretion events, refining and extending earlier gradient–assembly correlations (e.g. “Gaia–Sausage–Enceladus”-like progenitors, Belokurov et al. 2018; Helmi et al. 2018).

In the cluster regime, the TNG-Cluster project (Nelson et al. 2024) opens the door to statistical studies of BCGs+SHs+ICL within the same galaxy-formation model as IllustrisTNG. First results map stellar/ICM properties and assembly histories, providing a framework to trace ex-situ build-up and outer-envelope growth at high masses. Complementary large-volume and comparison projects strengthen these trends. In The Three Hundred hydrodynamical simulations (Cui et al. 2018), the ICL fraction correlates with the cluster dynamical state, supporting a picture where late-time accretion and tidal processing grow diffuse outer components—an inference directly relevant to massive-galaxy SHs and their metallicity gradients in dense environments (Contreras-Santos et al. 2024). At group/cluster scales in TNG300 (Nelson et al. 2019), recent work revisits BCG growth and the timing of ex-situ assembly, highlighting late-time outer-envelope build-up and providing predictions for metallicity and age trends with radius that can be confronted with deep imaging and spectroscopy (Montenegro-Taborda et al. 2023).

Finally, related zoom studies continue to clarify the in-situ vs. accreted imprint on chemo-kinematics. Edge-on maps in AURIGA connecting age–metallicity– $[\alpha/\text{Fe}]$ to merger-driven heating offer templates for interpreting thick-disc/inner-halo overlaps and their projected gradients. These maps emphasize that spherically averaged metallicity profiles are intrinsically steeper

than minor-axis projections typically measured observationally (Pinna et al. 2024).

In this paper, we expand upon the analysis presented in Contini et al. (2024d), where we first implemented SH formation in our semianalytic model of galaxy formation. Here, we investigate the main scaling relations between SH and BCG–ICL mass, and between SH mass and the transition radius in the first part, followed by an analysis of their colours and metallicities in the second part, as a function of redshift from $z = 2$ down to the present time.

The remainder of the paper is structured as follows. In Section 2, we describe the implementation of SH formation in our model and provide details about the simulations and the accompanying observational data. In Section 3, we present our analysis, highlight and discuss the main results. Finally, in Section 4, we summarize the key conclusions. Unless otherwise stated, stellar and halo masses are corrected for $h = 0.68$, and stellar masses are derived assuming a Chabrier initial mass function (Chabrier 2003).

2. Methods

For the analysis that follows in Section 3, we take advantage of the state-of-the-art semianalytic model FEGA25 (Formation and Evolution of GALaxies), in its latest version as detailed in Contini et al. (2025b), specifically with the AGNeject1 option for the hot gas ejection mode driven by active galactic nuclei (AGN) feedback (see Contini et al. 2025a for further details). FEGA25 implements updated prescriptions for baryonic physics, including positive AGN feedback, a renewed supernova (SN) feedback scheme, and a more sophisticated star formation law (Contini et al. 2024d).

2.1. Semi-analytic model and ICL formation

Since the key focus of this work is the redshift evolution of the main properties of SHs, we begin with a detailed description of their formation. Because SHs originate from the diffuse light, or ICL, we first provide a brief summary of its formation. In FEGA25, the ICL arises through several channels, whose relative importance varies across its assembly history. The three main channels are stellar stripping, mergers, and pre-processing. Stellar stripping of satellite galaxies contributes a significant fraction of diffuse light, as stars are removed from satellites due to the potential well of the host halo. In some cases, albeit less common, tidal forces can be strong enough to completely disrupt a satellite galaxy.

Another important channel is represented by mergers between central and satellite galaxies, both minor and major. At each merger event, the code assigns a fraction of the satellite’s stars to the ICL component associated with the central galaxy, with an average of 20% and a scatter of $\pm 5\%$. The last, channel is pre-processing, which can be considered a sub-channel, since pre-processed ICL ultimately originates from either stellar stripping or mergers (or both). In short, pre-processed diffuse light forms in halos other than that of the central galaxy and is subsequently accreted when those halos merge with the host.

In Contini et al. (2024a), and previously also in Contini et al. (2023), we showed that stellar stripping is the dominant channel of ICL formation, while mergers play a secondary role. However, as repeatedly discussed in earlier works, the net balance between the two channels strongly depends on the definition of mergers (see, e.g., Contini et al. 2018 for a detailed discussion, as

well as Joo et al. 2025 and Gendron & Martel 2025 for comparisons). We stress here that, in the model, the ICL is a physically motivated component whose mass and spatial distribution are determined by the cumulative effects of these processes along the halo assembly history, and not imposed by construction.

2.2. Definition of the stellar halo and transition radius

In FEAGA25, the SH forms directly from stars originally belonging to the ICL. The first implementation was introduced in Contini et al. (2024b) through the definition of a transition region between the central galaxy (CG) and the ICL, itself defined as the stars lying within the transition radius R_{trans} . This radius is linked to the halo concentration, which is computed on the basis of a Navarro-Frenk-White (NFW) dark matter distribution (Navarro et al. 1997). The ICL concentration is directly tied to halo concentration via the following equation:

$$c_{\text{ICL}} = \gamma c_{200} = \gamma \frac{R_{200}}{R_{s,\text{DM}}} = \frac{R_{200}}{R_{s,\text{ICL}}}, \quad (1)$$

where R_{200} and $R_{s,\text{DM}}$ represent the virial and scale radii of the DM halo, respectively, $R_{s,\text{ICL}}$ is the scale radius of the ICL mass distribution, and γ is a parameter quantifying how much more concentrated the ICL is relative to the DM. This parameter was calibrated in Contini et al. (2024b) using a Markov chain Monte Carlo algorithm, and typically ranges between 1 and 3. This model assumes that the ICL distribution follows an NFW profile (see, e.g., Contini & Gu 2020 for further details), but with higher concentration. From Equation 1, the transition radius R_{trans} is then defined as

$$R_{\text{trans}} = \frac{R_{200}}{c_{\text{ICL}}}, \quad (2)$$

which is essentially the analogue of the NFW scale radius for the ICL.

To model the SH, we assume that all stars belonging to the ICL and lying within the transition radius form the SH, considered as an intermediate region between the CG and the ICL. It must be noted that this implementation does not explicitly determine whether these stars are gravitationally bound to the central galaxy. Consequently, the SH can be regarded either as a distinct third component of the BCG+SH+ICL system, or as a transition zone. Stars can move between the ICL and SH components, and in certain conditions they can migrate from the SH to the BCG. By construction, the SH mass is therefore closely linked to the ICL mass and spatial distribution. In particular, a correlation between SH and ICL mass is an expected outcome of the adopted definition, while the residual scatter reflects variations in halo concentration, ICL formation efficiency, and the detailed assembly history of the system.

Two additional criteria regulate this process. First, if the transition radius R_{trans} lies within the bulge radius, all SH stars within it are transferred to the bulge. Second, for stability reasons, the SH mass cannot exceed the stellar mass of the BCG (bulge+disk)¹. Any excess mass in the SH is redistributed to the BCG's disk. These stability criteria imply that the SH mass is not a fixed fraction of the ICL mass, even at fixed halo mass or concentration, and introduce physically motivated scatter in all SH-related scaling relations.

As highlighted above, the SH stars may or may not be bound to the central galaxy. In the first case, the SH can be interpreted

¹ Bulge and disk formation and evolution are implemented in FEAGA as done in (Guo et al. 2011)

as a third component of the BCG+SH+ICL system, while in the second case—or in the mixed case with both bound and unbound stars—it represents a transition region between the galaxy and the surrounding ICL. Following Contini et al. (2024b), where SHs were first implemented, in this work we adopt the latter interpretation. Thus, the system is modelled as a central galaxy, consisting of bulge and disk, surrounded by a SH, all embedded in a more extended diffuse light component (see Figure 1 for a schematic illustration). We therefore emphasize that the interpretation of SHs as transition regions is a direct consequence of the adopted definition, while the quantitative trends in their mass, structure, and stellar populations explored in Section 3 reflect genuine physical dependencies on halo concentration, ICL assembly, and satellite accretion.

Although the definition of the transition radius is somewhat arbitrary, in Contini et al. (2024b) we showed that the typical values of R_{trans} for halos of given mass are consistent with both observations and theoretical predictions, such as the relation found by Proctor et al. (2024). It is also worth discussing an important caveat. The observational definition of the SH is not unique. Historically, the integrated light profiles of the Milky Way and other disk galaxies were successfully fit by a de Vaucouleurs component dominating both the central regions and the outskirts, which led to the interpretation of the SH as a photometric extension of the bulge (e.g., de Vaucouleurs 1959). A purely morphological classification does not capture the physical distinctiveness of the halo, whose stars typically exhibit low metallicities, dispersion-dominated kinematics, and signatures of accretion and minor merging (e.g., Carollo et al. 2007; Carollo et al. 2010; Helmi 2008; Deason et al. 2013; Belokurov et al. 2020). This is particularly clear in the Milky Way, where Gaia has revealed that a significant fraction of the inner halo originates from a major accretion event (Gaia-Enceladus; Helmi et al. 2018; Belokurov et al. 2018), and where chemical and kinematic surveys identify multiple substructures and a dual-halo configuration. In this work we therefore adopt a physical definition of the SH, based on dynamical selection criteria rather than on a decomposition of the light profile alone. This approach reflects modern observational evidence that the halo traces the hierarchical assembly history of the host galaxy, and is distinct from bulge and disk components both in origin and in stellar population properties (e.g., Gallart et al. 2019; Naidu et al. 2020).

2.3. Stellar populations: colours and metallicities

The model tracks the age and metallicity of the stellar populations associated with each stellar component (BCG, SH, and ICL) by following their star-formation and chemical-enrichment histories self-consistently within the semi-analytic framework. Broad-band colours are computed by applying stellar population synthesis models to the predicted stellar mass, age, and metallicity of each component, assuming a Chabrier initial mass function.

In this approach, colours and metallicities are not free parameters tuned to reproduce the observations, but are direct outputs of the model, inherited from the formation histories of the different stellar components. In particular, the SH and the ICL are assumed to evolve passively after their formation, with no *in situ* star formation, consistently with their predominantly accreted origin.

Mean metallicities are derived using the same mass-weighting scheme adopted for the computation of colours, ensuring a coherent mapping between the semi-analytic outputs and the observable quantities used in the comparison with data.

Table 1. Name of the simulation (first column), box size (second column), resolution (third column) and thresholds in selecting dark matter halos (fourth column).

Name	L [Mpc/h]	Resol. [M_{\odot}/h]	Thresh. [M_{\odot}/h]
YS300	300	$2.2 \cdot 10^9$	$> 10^{14}$
YS200	200	$3.26 \cdot 10^8$	$> 10^{13}$
YS50HR	50	10^7	$> 10^{12}$

While stellar populations represent one of the most challenging aspects to model within a semi-analytic framework, this methodology allows us to perform a physically motivated and internally consistent comparison between model predictions and observations.

In the remainder of this section, we briefly describe the merger trees (Section 2.4) and the observational data set (Section 2.5) before moving on to the analysis and discussion of the main results.

2.4. Merger trees

In order to construct galaxy catalogs, semianalytic models require merger trees extracted from dark matter–only numerical simulations. For this purpose, we employ a set of three cosmological simulations carried out with the latest version of the GADGET code, namely GADGET-4 (Springel et al. 2021). These simulations span different volumes and mass resolutions, as summarized in Table 1, and the corresponding merger trees have been used to generate the inputs for FEGA25.

All runs adopt the same comoving gravitational softening length of $3 \text{ kpc}/h^2$, and follow the Planck 2018 cosmology (Planck Collaboration et al. 2020): $\Omega_m = 0.31$ for the matter density parameter, $\Omega_{\Lambda} = 0.69$ for the cosmological constant, $n_s = 0.97$ for the primordial spectral index, $\sigma_8 = 0.81$ for the power spectrum normalization, and $h = 0.68$ for the dimensionless Hubble parameter. The simulations were evolved from an initial redshift of $z = 63$ down to the present day, with data stored in 100 snapshots uniformly distributed in cosmic time between $z = 20$ and $z = 0$.

We note that numerical resolution can play an important role when the same halos are simulated at different resolutions, particularly for quantities related to satellite survival, stripping, and mass loss (e.g. Contini et al. 2014). However, this effect has been explicitly tested in previous work, where we verified that, in the halo-mass ranges where different simulations overlap, the predicted properties of diffuse stellar components are consistent within the intrinsic scatter. Nevertheless, in Appendix A we provide some additional plots, separating the data coming from the different runs.

Because of the different resolutions of the simulations, we impose distinct mass thresholds when selecting dark matter main halos (focusing exclusively on centrals), as listed in Table 1. The largest volume run, YS300, provides a statistically signif-

² Within the semi-analytic framework adopted here, the gravitational softening length does not directly affect the predicted galaxy structural properties, which are computed analytically rather than resolved numerically. To further minimize resolution-driven effects, each simulation is therefore used only within the halo-mass regime where it provides a reliable sampling of the underlying population, and no direct comparison of the same systems across different resolutions is performed in this work.

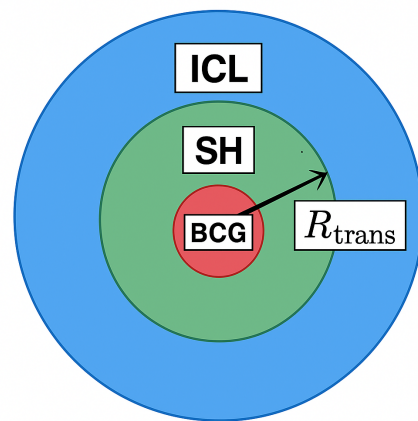


Fig. 1. Schematic representation of central galaxies and their surrounding stellar halos and intracluster stars. The stellar halo is defined as the stellar component within the transition radius R_{trans} , marking the intermediate region between the galaxy and the intracluster light.

icant sample of massive groups and clusters, while the highest-resolution box enables us to probe Milky Way–sized halos. This combined catalog forms the basis for the analysis presented in Section 3.

2.5. Observed data

To compare the predictions of our model with observational data, we make use of the survey VEGAS (Capaccioli et al. 2015; Iodice et al. 2021) and the Fornax Deep Survey (FDS; Iodice et al. 2016). These surveys do not provide metallicity measurements. Therefore, for the same targets, we complement them with data from the Fornax3D project (F3D; Sarzi et al. 2018) and the M3G survey (Krajnović et al. 2018). Throughout the rest of the paper, we refer to this combined dataset simply as VEGAS, which includes both colours and metallicity information.

VEGAS is a wide-field deep imaging program conducted with the VLT Survey Telescope (VST) at ESO’s Paranal Observatory. Its primary aim is to explore the faint outskirts of nearby ETGs down to very low surface brightness levels, typically reaching $\mu_g \sim 28.5\text{--}29 \text{ mag arcsec}^{-2}$ (Iodice et al. 2021). By combining multi-band wide-field and deep optical imaging (u, g, r, i), VEGAS allows for a detailed study of the structural properties and stellar populations in the outer regions of galaxies, unveiling faint SHs, extended envelopes, and substructures such as shells, streams, and tidal debris, which are relics of past accretion and merging events (Mihos et al. 2017).

In addition, VEGAS plays a crucial role in the investigation of the ICL. This component provides direct constraints on the assembly history of massive structures and the efficiency of tidal stripping and galaxy interactions (Contini et al. 2014; Montes & Trujillo 2018; Spavone et al. 2020). By building a statistical sample of ETGs across diverse environments, from isolated systems to dense clusters, VEGAS delivers a key observational benchmark for hierarchical galaxy formation models and for the study of the stellar mass assembly at large radii (Cooper et al. 2010; Pillepich et al. 2018). For further details and references about the survey, we refer the reader to Contini et al. (2024b).

The Fornax Deep Survey (FDS) is a deep optical imaging program carried out with the VST as part of the VEGAS collaboration. Its main goal is to map the entire Fornax cluster down to unprecedented surface-brightness levels of about $\mu_g \sim 29 \text{ mag}$

arcsec⁻², thus providing the first homogeneous and contiguous photometric coverage of both the cluster core and its periphery (Iodice et al. 2016). With a wide field of view of one square degree per pointing and multi-band coverage (u, g, r, i), FDS enables a systematic exploration of the galaxy population of Fornax, ranging from early- and late-type systems to ultra-diffuse galaxies and low-surface-brightness dwarfs (Venhola et al. 2017; Venhola et al. 2018).

A key strength of FDS is its ability to trace the ICL and the extended stellar envelopes of massive galaxies, which represent direct evidence of the cluster’s ongoing assembly and provide insights into tidal stripping, galaxy harassment, and merging processes (Iodice et al. 2017; Spavone et al. 2017). Moreover, by resolving faint structural and colour gradients across galaxies, the survey constrains the stellar populations and metallicity distributions, thereby shedding light on environmental transformation processes and their role in shaping galaxy evolution within dense environments.

FDS stands as one of the deepest wide-area optical surveys of a nearby cluster, complementing similar campaigns in Virgo and Coma. By simultaneously resolving the brightest galaxies and the faintest dwarf systems, it delivers a comprehensive view of galaxy evolution in clusters and offers crucial observational constraints for cosmological models of structure formation (Drinkwater et al. 2001; Capaccioli et al. 2015). For further details about FDS we refer the reader to Iodice et al. (2016).

We note that, while VEGAS primarily targets bright central galaxies, the FDS sample includes a significant fraction of satellite systems. For this reason, FDS data are not used here as a direct counterpart of the simulated sample, which includes only central galaxies. Instead, FDS provides a complementary reference for the properties of diffuse outer stellar components in a dense cluster environment. The comparison with model predictions is therefore statistical in nature and is not intended as a one-to-one correspondence between individual observed and simulated systems. This comparison therefore provides a consistency check on the typical scales and trends of diffuse stellar components, rather than a direct test of individual galaxy properties. In the following analysis, we remind the reader that we combine VEGAS-FDS-F3D-M3G data and, for simplicity, refer to the entire dataset as VEGAS in the discussion, but we separate them in the analysis where VEGAS data alone will be indicated as VG.

For the full sample of galaxies, we consider the $g-r$ and $r-i$ colours. Moreover, we define two transition radii, R_1 and R_2 , as the radii at which the second and third components of the 1D surface-brightness profile fits begin to dominate over the first and second components, respectively. In this work, when comparing with the model-defined transition radius, we adopt R_2 , which marks the transition between the accreted bound and the diffuse unbound stellar components. This choice is motivated by the fact that R_2 represents the most appropriate observational analogue of the SH-ICL boundary probed by the semi-analytic model. Not having the $g-r$ or $r-i$ colours available for all targets (for around 40% of them), nor the second transition radius R_2 (for around 20% of them), we adopted an empirical calibration strategy based on a subset of galaxies for which both radii and multi-colour photometry were available. Specifically, we proceeded as follows:

1. Training sample.

From the galaxies with both R_1 and R_2 measured, we converted angular radii from arcminutes into arcseconds (and subsequently into kiloparsecs at the distance of the Fornax

cluster, assuming $1'' \simeq 0.097$ kpc at 20 Mpc). Missing photometric values in the $g-r$ and $r-i$ colours were treated via a bootstrap imputation scheme (Efron 1979):

- If one colour was available, the other was inferred from a linear regression relation calibrated on galaxies with both colours, adding scatter consistent with the observed residuals.
- If both colours were missing, we imputed values from the bootstrap distribution of the sample mean.

This procedure, repeated for 5000 bootstrap resamplings, provided a median estimate together with 16th–84th percentile intervals for each imputed value.

2. Empirical $R_1 \rightarrow R_2$ mapping.

We modeled the correlation between the two transition radii in logarithmic space,

$$\log_{10} R_2 = a + b \log_{10} R_1,$$

and calibrated the parameters (a, b) from the training sample³. A bootstrap approach (5000 realizations) was used to propagate both coefficient uncertainties and intrinsic scatter.

3. Application to target galaxies.

For observed galaxies with only R_1 , we predicted R_2 using the calibrated relation. Each prediction was expressed as a median with an associated 16th–84th percentile range, thus quantifying the uncertainty of the extrapolation. Alongside the structural radii, we retained the outer stellar metallicity to allow further analysis of correlations between halo properties and stellar populations.

3. Results and discussion

In the following, we present our analysis, which is organized into two main parts. In the first part, we examine the key scaling relations between the SH mass and the transition radius R_{trans} defined above, as well as with the masses of the BCG and the ICL. In this context, we also assess the role of halo concentration and the efficiency of ICL formation, two fundamental factors in shaping SHs. In the second part, we focus on the colours ($g-r$ and $r-i$) and metallicity of the three components (BCGs, SHs, and ICL). In both cases, we trace their redshift evolution from $z = 2$ to the present day.

3.1. Scaling relations

The transition radius R_{trans} is a fundamental quantity in defining SHs, particularly their mass, which also depends on the total stellar mass contained in the ICL. Importantly, R_{trans} is strongly determined by the ICL concentration, which in turn is tightly connected to the halo concentration. In the left panel of Figure 2, we show the SH mass as a function of R_{trans} at different redshifts (colours as indicated in the legend). The dashed lines represent the 16th and 84th percentiles of the distribution at $z = 0$. The figure reveals that this relation depends only weakly on redshift: only the $z = 2$ curve falls outside the upper percentile envelope of the $z = 0$ distribution.

Interestingly, at fixed R_{trans} , the SH mass increases with redshift. A constant transition radius implies the same ICL concentration, and a halo concentration that is a factor γ (between 1 and

³ The adoption of a power-law relation between R_1 and R_2 is motivated by the fact that both quantities trace characteristic transition scales in multi-component surface-brightness profiles and are therefore expected to scale approximately proportionally in logarithmic space.

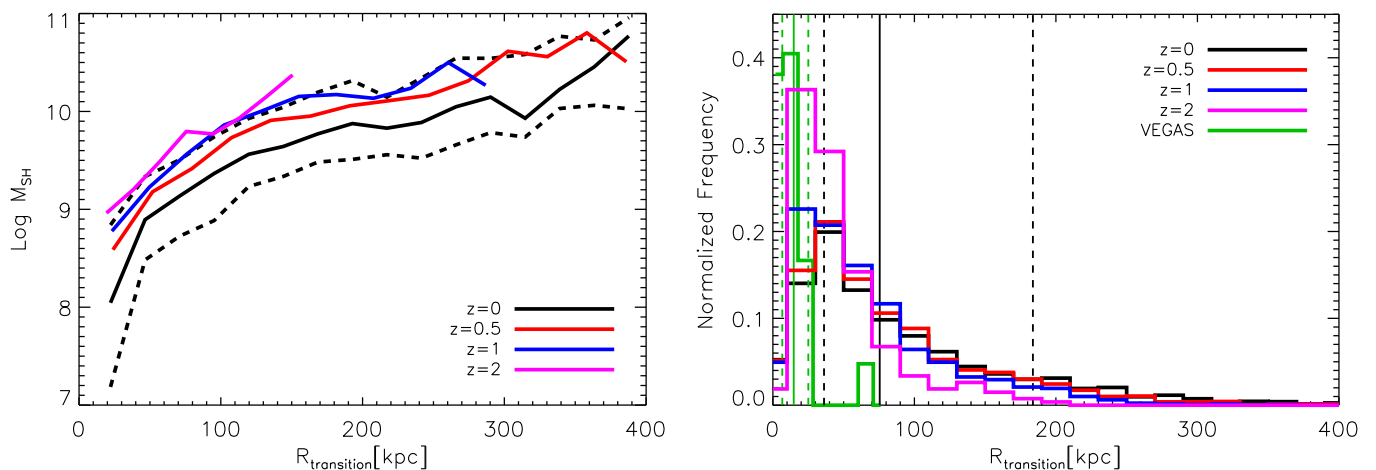


Fig. 2. Left panel: stellar halo mass as a function of the transition radius R_{trans} , at different redshifts as indicated in the legend. The two black dashed lines represent the 16th and 84th percentiles of the distribution at $z = 0$. At fixed R_{trans} , the stellar halo mass increases slightly with redshift, since dark matter halos with similar concentrations are more evolved at earlier epochs than at later times. Right panel: Distribution of transition radii at different redshifts (different colours) and as inferred from observations (VEGAS, green line). The model distributions extend to systematically larger values of R_{trans} than the observational one, while the VEGAS distribution is more narrowly peaked at smaller radii (see the vertical lines indicating medians, 16th and 84th percentiles of the distributions for the model predictions at $z = 0$ (black) and VEGAS (green)). This offset reflects the different definitions adopted in the SAM and in observations, as well as differences in sample selection. The comparison should therefore be interpreted in a statistical sense, focusing on typical scales and trends rather than on a one-to-one correspondence. Across all redshifts, the majority of model transition radii lie within ~ 100 kpc, with a tail extending to larger values in the most massive systems.

3; see Section 2) lower. Given the halo mass–concentration relation (e.g., Prada et al. 2012; Correa et al. 2015; Child et al. 2018), this suggests that BCG host halos at different epochs may exhibit similar concentrations within the intrinsic scatter of the relation. At higher redshift, such concentrations correspond to dynamically more evolved halos, which likely produced a substantial amount of ICL, part of which is converted into significant SH mass. We verified this scenario by selecting samples of halos at $z = 2$ and comparing them with their $z = 0$ counterparts at fixed R_{trans} , finding that this trend is indeed statistically robust.

Another point worth stressing is that R_{trans} can extend to very large scales: at $z = 0$ it can reach ~ 400 kpc in the most massive halos, while ~ 300 kpc at $z = 1$, and at $z = 2$ it still extends up to ~ 150 kpc. The systematic decrease of R_{trans} with redshift is a natural outcome of the hierarchical growth of structures: halos at higher redshifts are, on average, less massive and dynamically younger. At least at $z = 0$, where a comparison is possible, our results are in good agreement with those of Proctor et al. (2024), who analyzed the EAGLE (Schaye et al. 2015; Crain et al. 2015) and C-EAGLE (Bahé et al. 2017; Barnes et al. 2017) simulations using an independent definition of R_{trans} (Contini et al. 2024b).

The right panel of Fig. 2 shows the distribution of transition radii, R_{trans} , predicted by the model at different redshifts and inferred from the VEGAS observations. While the observational distribution is narrowly peaked at relatively small radii, the model predicts a broader distribution extending to systematically larger values, particularly at low redshift. This offset indicates that observationally defined transition radii, derived from multi-component photometric decompositions through minimization of the rms scatter of the fits (e.g. Seigar et al. 2007), and shown to correlate with changes in surface-brightness, ellipticity, position angle and colour profiles (Spavone et al. 2017, 2021), do not necessarily trace the same physical boundary as the model-

defined R_{trans} , which separates stars bound to the central galaxy from the diffuse intracluster component.⁴

Part of the difference may reflect sample selection effects, as the observational data probe a restricted range of massive systems in the local Universe, whereas the model includes central galaxies spanning a wider range of stellar and halo masses. In addition, the heterogeneous distances of the VEGAS targets introduce an additional source of scatter in the conversion from angular to physical radii. For these reasons, the comparison between observations and model predictions should be interpreted in a statistical and qualitative sense, focusing on typical scales and trends rather than on a direct, one-to-one correspondence.

In Figure 3 we present the scaling relations between the SH and the BCG mass (left panel), and between the SH and the ICL mass (right panel), at $z = 0$. In both cases, circles are colour coded according to the halo concentration. We find that the SH mass correlates with both the BCG and the ICL mass, although the latter relation exhibits a significantly smaller scatter. This is not surprising, given that SHs form directly from stars belonging to the ICL, or because the SH is a tail of the ICL instead of a separate component. An important trend visible in both panels is that the SH mass tends to increase in less concentrated halos, which are also typically the most massive ones. At first sight, this might appear in tension with the results of Contini et al. (2023), who found higher ICL fractions in more concentrated halos. However, it should be stressed that our plots show mass-to-mass relations, not fraction-to-mass relations. Moreover, halo concentration is directly linked to the transition radius R_{trans} . Less concentrated halos (and their associated ICL) are characterized by larger values of R_{trans} (see Equation 2), which in turn implies a larger SH mass, depending on the amount of ICL already in place. The key message is therefore that halo concen-

⁴ For the observational comparison shown in Figure 2, we use the R_2 values derived from VEGAS, corresponding to the transition between the accreted bound and the diffuse unbound stellar components.

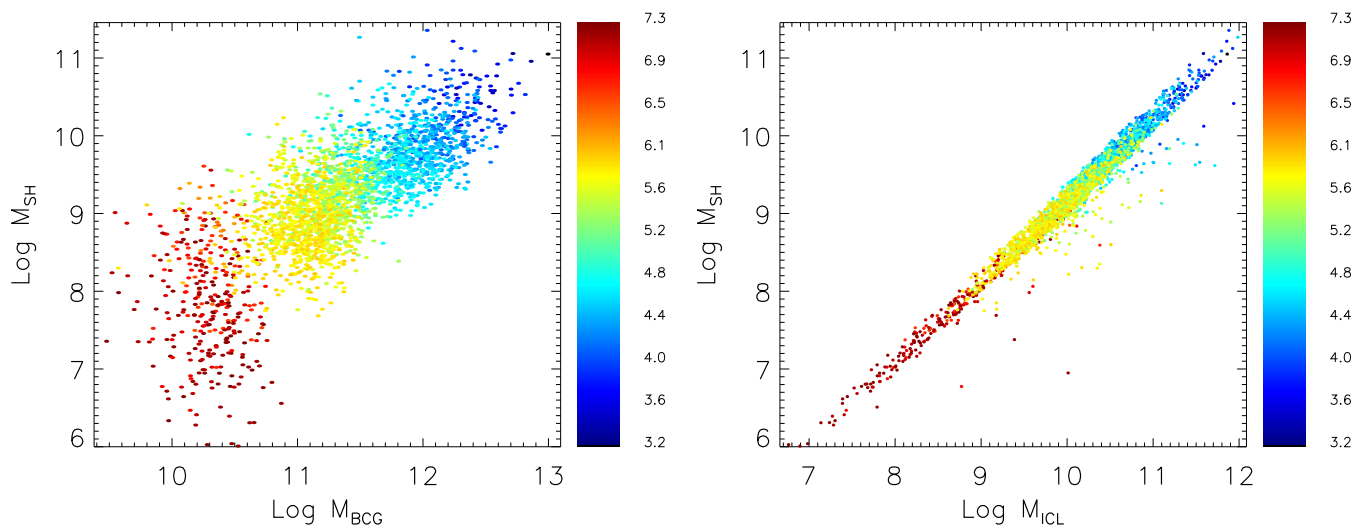


Fig. 3. Scaling relations between the mass of stellar halos and that of the associated central galaxy (left panel) and intracluster light (right panel). The colour bar encodes the dark matter halo concentration, with redder colours corresponding to higher concentrations. The stellar halo mass correlates well with both the BCG and the ICL mass, with a notably smaller scatter in the ICL case. In both relations, halo concentration plays a key role: stellar halos tend to be more massive in less concentrated dark matter halos, which are also the most massive systems.

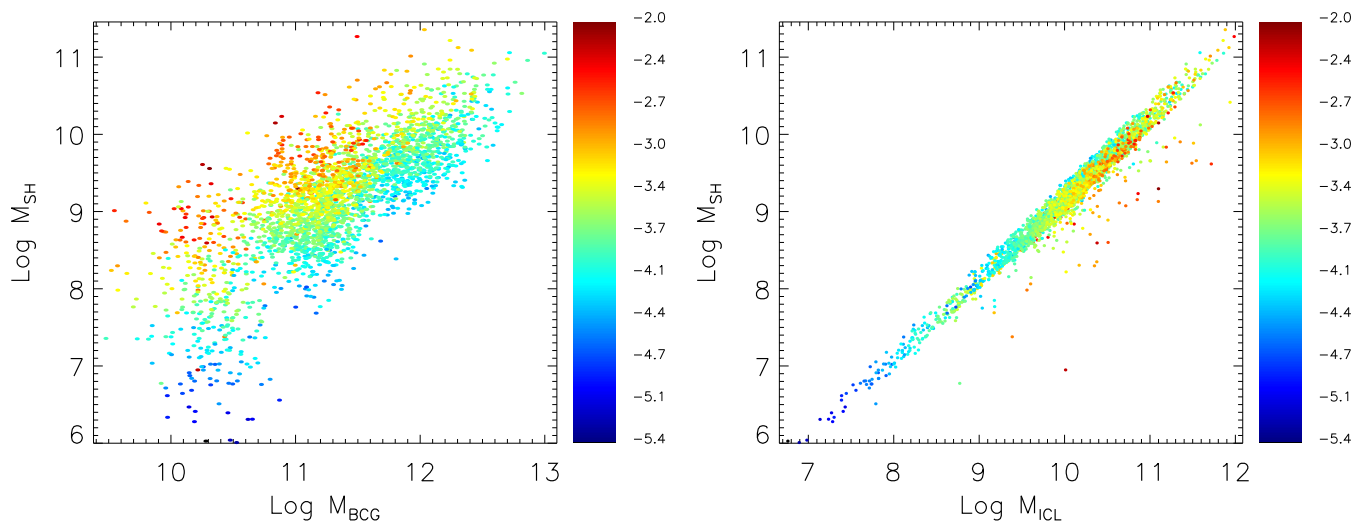


Fig. 4. Similar to Figure 3, the plots show the same scaling relations, but with the colour bar now indicating the logarithm of the efficiency of ICL production in dark matter halos. The efficiency is defined as the ratio between the ICL mass and the halo mass. A clear trend emerges in both panels: stellar halos tend to be more massive when the efficiency of ICL production is higher. In the left panel, this appears at fixed BCG mass, where redder colours correspond to more massive stellar halos, while in the right panel the trend follows the main relation itself.

tration, through its connection with the ICL concentration, plays a crucial role in shaping the formation of SHs.

Another striking feature is that both scaling relations appear nearly linear by eye. Focusing on the SH–BCG mass relation, we performed a simple linear fit in logarithmic space. The best-fit slope is 0.99, with a relatively small intercept of -2.07 , confirming that the relation is essentially linear. This allows us to reformulate the fit in terms of the mass fraction $f_{\text{SH-BCG}}$ on the y-axis, since the $f_{\text{SH-BCG}}$ –BCG mass relation is nearly constant. Within the range of $\log M_{\text{BCG}} = [9.5, 13]$, we obtain the following values: mean $f_{\text{SH-BCG}} = [0.0074, 0.0069]$, mean $+1\sigma = [0.0158, 0.0174]$, mean $-1\sigma = [0.0034, 0.0028]$, mean $+2\sigma = [0.0347, 0.0427]$, and mean $-2\sigma = [0.0016, 0.0011]$. These predictions compare very well with the observed data from Merritt et al. (2016) (their Figure 5, left panel) and Gilhuly et al. (2022)

(their Figure 7). Both works are based on the Dragonfly Survey, with Gilhuly et al. extending the analysis to lower-mass galaxies than Merritt et al. Specifically, our $\pm 1\sigma$ region encompasses the bulk of the Merritt et al. data, with the exception of three outliers not even included within $\pm 2\sigma$. Similarly, for the Gilhuly et al. sample, our $\pm 1\sigma$ region accounts for most of their galaxies, while $\pm 2\sigma$ essentially covers the full set. This agreement provides strong support for the robustness of our SH implementation in FEAGA25.

While halo concentration is a fundamental driver of ICL and SH formation, another quantity that may play a role is the efficiency of ICL production. Intuitively, the larger the amount of ICL, the more likely it is to form massive SHs. We explore this aspect in Figure 4, which shows the same two relations as in Figure 3, but this time with circles colour coded by the ICL for-

mation efficiency. We define the efficiency as the ratio between the total ICL mass assembled up to a given epoch (here $z = 0$) and the total halo mass. As shown in Contini et al. (2024a), the efficiency of ICL formation is broadly halo-mass independent, although this does not necessarily preclude a role in SH growth.

Both panels in Figure 4 highlight a clear trend: SHs are more massive in systems with higher ICL formation efficiencies. This is most evident in the left panel, where at fixed BCG mass (and thus at approximately fixed halo mass within a range), redder circles indicate larger efficiencies. In the SH–ICL mass plane, the trend is somewhat less pronounced but still visible, with low-mass SHs corresponding to bluer (lower-efficiency) points, and high-mass SHs associated with redder ones. Taken together, halo concentration and ICL formation efficiency both emerge as key factors in shaping SH properties. We also emphasize that repeating this analysis at higher redshifts leads to no significant differences: the trends already hold at earlier times, with the expected variations in scatter due to number statistics.

Having explored these scaling relations, we now turn to more challenging properties to model in a semianalytic framework, namely colours and metallicities.

3.2. Colors and metallicity

Figure 5 shows the $g-r$ and $r-i$ diagram for BCGs (red), SHs (black), and ICL (blue) for each individual system in our sample, as a function of redshift (different panels). We can see that there is a diversity of colours, spanning a wide range in both cases. Overall, it appears that all three components have similar colours, and independently of redshift, but also all of them progressively redden from high redshift to the present day. At $z = 0$, we compare our predictions with the observed SH colours from VEGAS (green diamonds for VG and brown squares for FDS). The uncertainties in the observational data are broad enough to encompass most of our predicted values, although the distribution appears somewhat more scattered. Nevertheless, the majority of the observed points fall within the cloud of model predictions. This is visible by eye when comparing the black triangle with error bars (indicating mean and $\pm 1\sigma$ distribution of the predicted SH colours). Once we consider $\pm 2\sigma$, most of the green diamonds and error bars fall within the predicted distribution.

In order to catch any possible difference between the colours of the different components, we plot in Figure 6 their distributions at $z = 0$ (left panel) and $z = 2$ (right panel). Solid lines represent the $g-r$, while the dashed ones indicate $r-i$, and line colours denote the three components as in the previous figure. Plotted together with our predictions at $z = 0$, we show the mean values of the two observed colours (thick green solid and dashed lines) along with their corresponding $\pm 1\sigma$ distributions (thin green solid and dashed lines).

There are several key points worth discussing, mainly in the difference between the two redshifts investigated. First of all, as already noted in Figure 5, both colours tend to become redder with time, which is a natural consequence of ageing. For SHs and ICL it is understandable since they do not have any star formation, and ageing overcomes the newly stripped stars that might be blue. For the BCGs instead, it just means that they age by passive evolution with little episodes of star formation, after a period of growth due to mergers (e.g., Oliva-Altamirano et al. 2014; Lee & Yi 2017 or Contini et al. 2024c for a review), and the fact that $g-r$ grows faster than $r-i$ is a clear indication of that.

Another important feature of the plot is that at $z = 0$ all components and for both colours, have narrower distributions than those at $z = 2$, and with more pronounced peaks. This highlights

the variety of the populations at high redshifts with respect to an old population at the present day. Not only, at $z = 0$ the distributions appear to be alike, while that is not the case at $z = 2$. At this redshift, when the Universe was just 3 Gyr old, BCGs are consistently redder than the other two components. This trend is seen even at $z = 0$, but in a lesser degree, meaning that SHs and ICL age faster than BCGs. Again, this is understandable given the fact that star formation is not happening in these two components. More importantly, the model predictions for both colours show excellent agreement with the observed SH colours.

To summarize, our model predicts a negative gradient in colours from the inner component, the BCG, to the outer component, the ICL, but this trend weakens over time. Moreover, there is not statistical distinction between SHs and ICL, implying that they have very similar colours at any time. Once again, this can be explained by the tight link between the components, given that SHs form directly from stars originally belonging to the ICL.

Taken together, our results indicate that broadband colours alone are insufficient to disentangle SHs from the surrounding ICL: the two components display virtually indistinguishable $g-r$ and $r-i$ distributions at all epochs, while BCGs remain only mildly redder on average by $z = 0$. This degeneracy is physically expected if SHs are continuously replenished by the same accreted populations that build the ICL, and it is consistent with the large object-to-object scatter in observed colour gradients reported for nearby halos and extended envelopes (e.g. Merritt et al. 2016; Gilhuly et al. 2022). In the Local Group, both the Milky Way and M31 show negative colour/metallicity gradients in their outskirts, but with amplitudes that strongly depend on each system’s recent accretion history (Kalirai et al. 2006; Gilbert et al. 2014; Deason et al. 2014). Cosmological simulations likewise predict broadly similar colours for ex-situ dominated components—outer BCG envelopes, SHs, and ICL—modulated by the stochastic contribution of a few massive progenitors (Pillepich et al. 2018; Monachesi et al. 2019; Elias et al. 2020; Wright et al. 2024). Practically, our findings imply that future wide-field programs (e.g. LSST imaging combined with WEAVE/4MOST spectroscopy) should rely on chemo-dynamical tracers rather than broadband colours alone to unambiguously separate SHs from the diffuse intracluster population (Cooper et al. 2011; Helmi 2020; Spavone et al. 2020, 2021, 2022; Iodice et al. 2016).

By focusing on the metallicity of the three components, we can assess whether the trends observed for colours are also present in the metallicity distributions. In Figure 7, we plot the metallicity of the three components of each system in our sample, as a function of their radius and at the usual redshifts (different panels). The coloured rectangles show the 16th and 84th distribution for each component. The predictions at $z = 0$ are accompanied by observed SH metallicities from FDS (brown squares) only, because for VG they are not available. Before delving into the features of the plot, it is worth explaining how we calculate the radius of each component, in order to place them in the plot. In the case of the BCG, its radius is defined as done in Contini et al. (2019), mass-weighting the bulge and disk radii, i.e.:

$$R_{\text{BCG}} = \frac{R_{\text{bulge}} \cdot M_{\text{bulge}}^* + 1.68 \cdot R_{\text{sl}} \cdot M_{\text{disk}}^*}{M_{\text{BCG}}^*}, \quad (3)$$

where R_{bulge} and $1.68 \cdot R_{\text{sl}}$ are the half stellar mass radii of the bulge and disk, M_{bulge}^* , M_{disk}^* and M_{BCG}^* are the stellar masses of the bulge, disk and BCG as a whole, respectively. SHs are

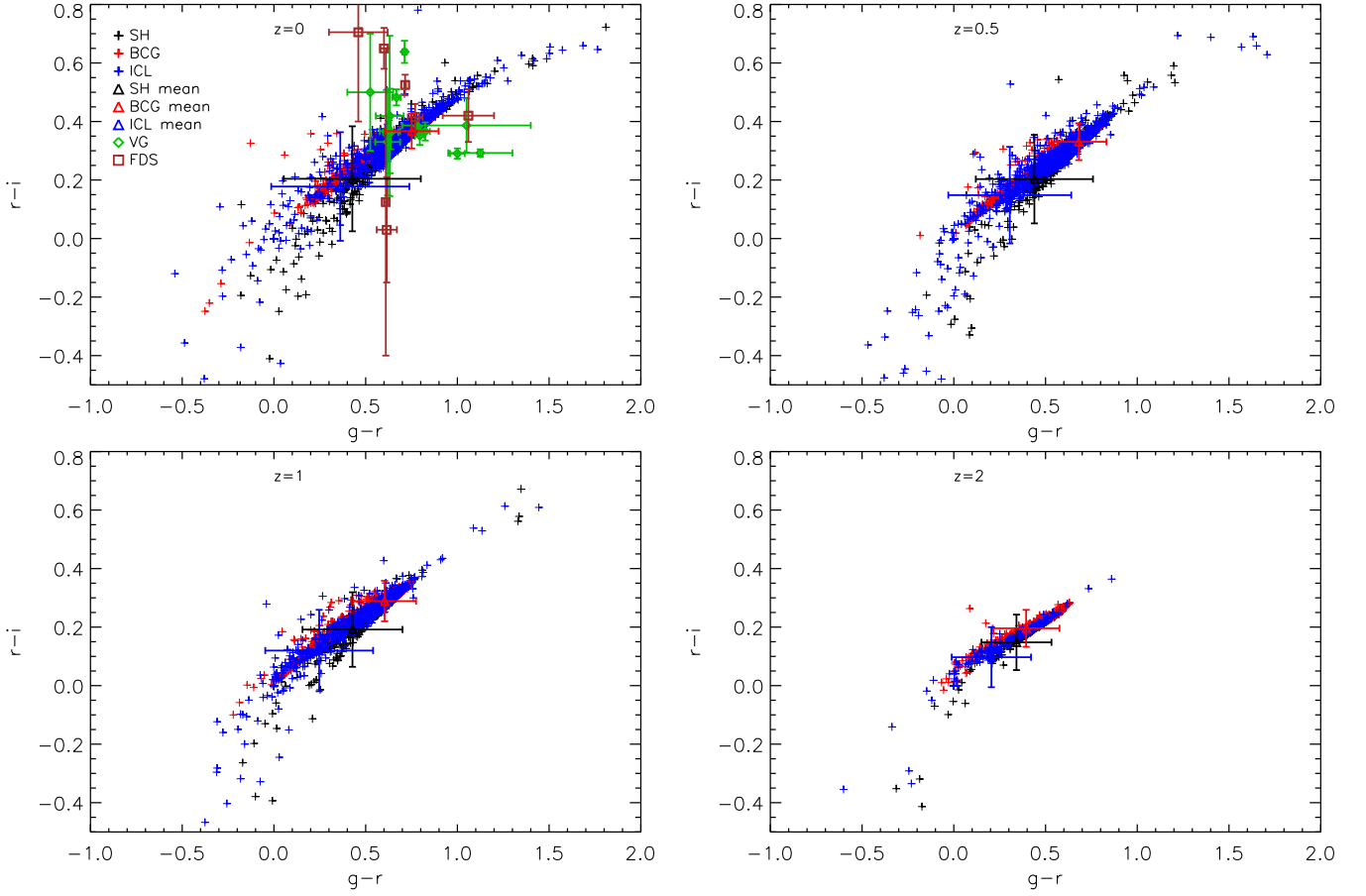


Fig. 5. Relation between $g-r$ and $r-i$ colours for the BCGs (red), stellar halos (black), ICL (blue) at different redshifts (separate panels), and as observed in VEGAS (green diamonds for VG and brown squares for FDS, at $z = 0$). Overall, the three components exhibit comparable colours, largely independent of redshift, and all progressively redden (shifting towards the right side of the diagrams) as the redshift approaches the present epoch.

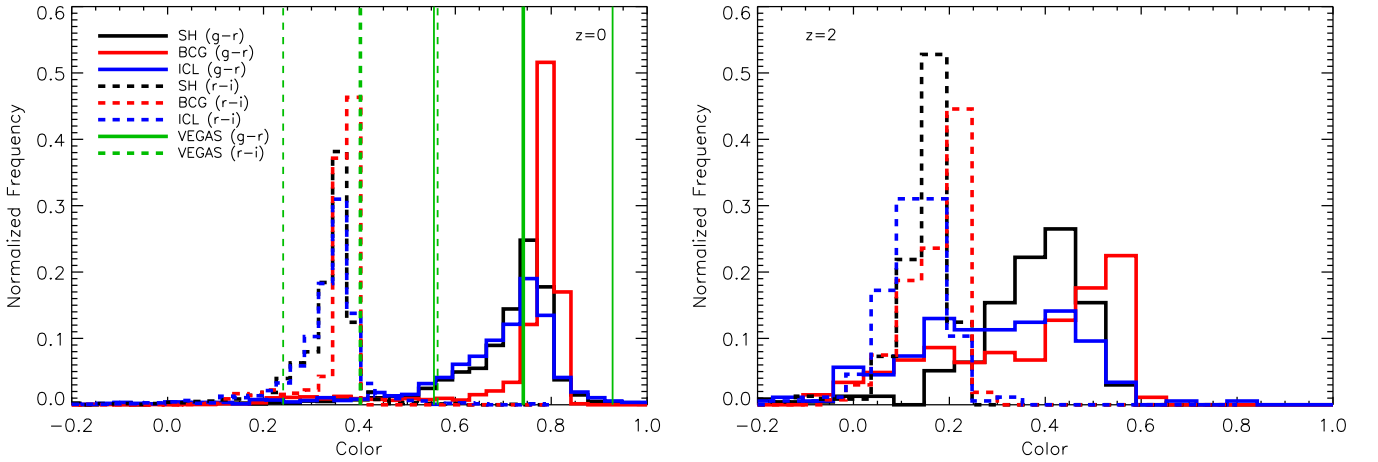


Fig. 6. For the same colours shown in the previous figure, the plots illustrate their distributions for each component at $z = 0$ (left panel) and $z = 2$ (right panel). As discussed above, both colours become redder with time, but the distributions reveal notable differences. At $z = 0$, the BCGs display narrower distributions with a more pronounced peak, while at $z = 2$ their distributions appear quite different. Overall, stellar halos and the ICL exhibit similar distributions at $z = 0$, whereas at $z = 2$ they are statistically distinct. Importantly, BCGs are consistently redder than the other two components, independent of redshift. The green thick lines (solid and dashed) represent the mean colours observed in VEGAS (VG+FDS), while the thinner ones indicated the $\pm 1\sigma$ distribution. The predicted $g-r$ and $r-i$ of the SHs at $z = 0$ are very close to the observed ones.

defined in terms of the transition radius R_{trans} ; accordingly, we place them at half of this radius. Similarly, for FDS data we place them at $R_2/2$. For the ICL instead, there is no clear place-

ment because, in principle, they can extend up to the virial radius. Considering that the "real" radius has no physical impact in the context of this plot, we place the ICL to $2 \cdot R_{\text{trans}}$.

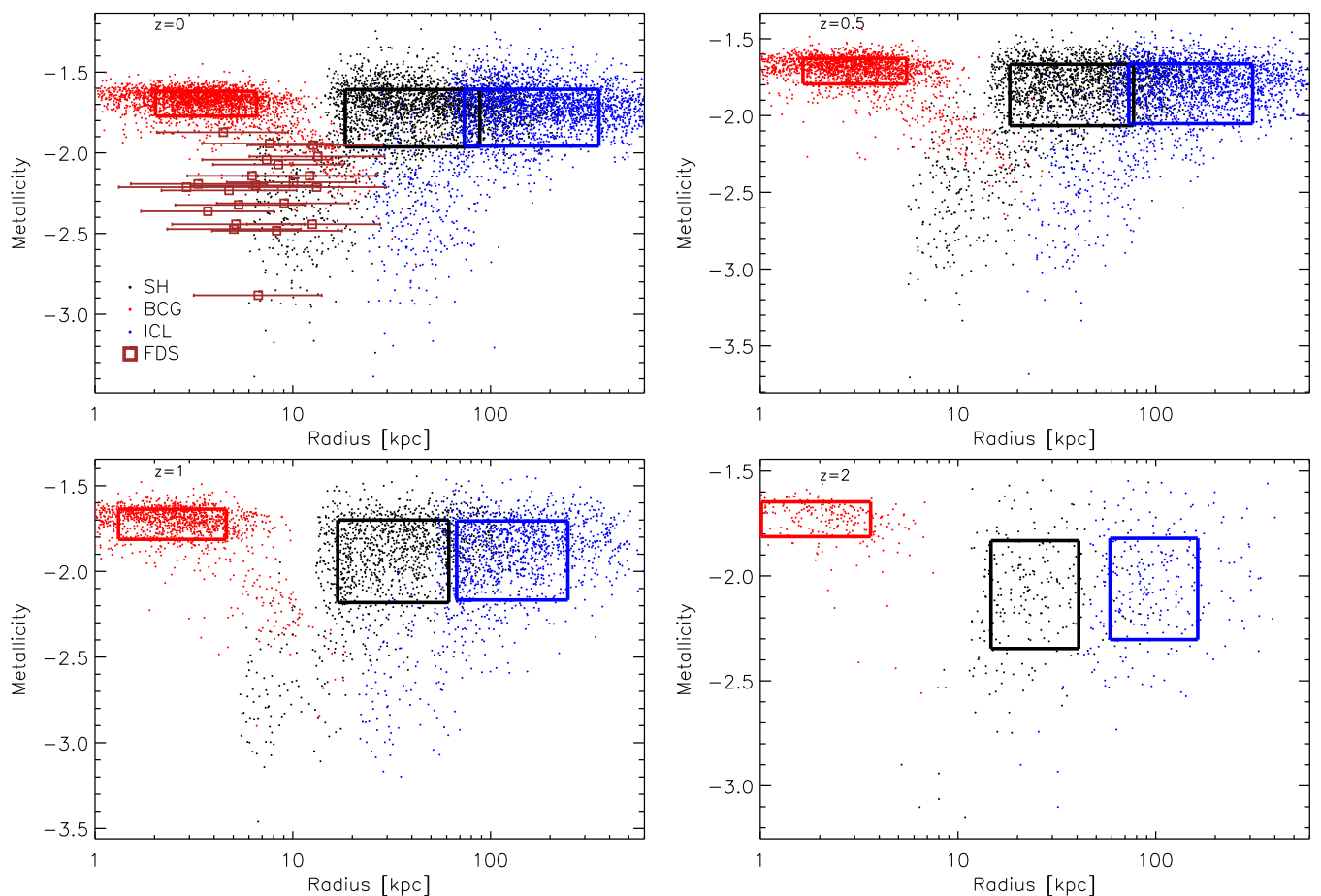


Fig. 7. Metallicity profiles ($\log Z$) of the three components as a function of radius (see text for details), shown at different redshifts (separate panels). At high redshift, both stellar halos and the ICL tend to be more metal-poor than the BCGs, although this trend becomes less evident at lower redshifts. The shaded rectangles mark the regions enclosing the 16th to 84th percentiles of the distributions, while brown squares represent the observed metallicities in FDS at $z = 0$.

The plot shows us that both SHs and ICL are more metal poor than the BCGs at high redshift, but the gap becomes smaller approaching redshift $z = 0$, where the difference in metallicity between the three components is indistinguishable. Not only, SHs and ICL have the same metallicity independently of the redshift. FDS data lie within the cloud of predicted SH metallicities on the left side of the panel, closely tracing the BCG distribution. This behavior likely arises from two factors: first, the observationally defined R_2 differs intrinsically from our model definition of R_{trans} , though the two are physically related; second, while our analysis focuses on central galaxies in the SAM, the FDS sample mainly consists of satellites, which are on average less massive than the model centrals.

As done above with colours, we need to quantify in a better way the real difference, if any. So, we plot in Figure 8 the metallicity distributions of BCGs, SHs and ICL, at $z = 0$ (left panel) and $z = 2$ (right panel). By focusing on $z = 2$, we can see that, while the metallicity distributions of SHs and ICL are very similar, almost identical, that of BCGs is very much different and peaks on higher metallicity. The peak for the BCGs is at ~ -1.7 , while those of SHs and ICL is wide, between ~ -2.0 and ~ -2.3 , on average at -2.15 . Hence, the gap in metallicity between BCGs and SH-ICL is around 0.4 dex at $z = 2$.

At $z = 0$, the picture is rather different. The three distributions are very similar, although those of SHs and ICL are wider. Considering the peaks, the average metallicity of BCGs does not

change with respect to that at $z = 2$ (~ -1.7), but SHs and ICL become more metal rich as time goes by, almost reaching the average metallicity of BCGs. The gap between the mean metallicity of BCGs and that of SHs-ICL is around 0.1 dex. As noted above—and therefore expected—the FDS SH metallicity distribution peaks at systematically lower values than our predictions, suggesting that these SHs likely originate from disrupted dwarf galaxies, as noticed in Section 1.

To summarize, similarly to colours, our model predicts a negative gradient from the BCG to the ICL, which is very clear at high redshifts, but almost flattens over time. Again, as for the colours, SH and ICL have the same metallicity.

The redshift evolution of metallicity strengthens the above picture. At $z = 2$ we find a ≈ 0.4 dex offset between BCGs and the SH-ICL pair, with the latter two being essentially indistinguishable; by $z = 0$ the gap shrinks to ≈ 0.1 dex as SHs and the ICL become more metal rich. This convergence naturally arises if late-time growth in the outskirts is increasingly driven by the stripping of relatively massive, chemically evolved satellites, while early assembly is dominated by lower-mass, metal-poor dwarfs. The trend echoes simulation results in which ex-situ accretion builds extended BCG envelopes at late times and predicts shallow, slowly evolving outer metallicity gradients (Nelson et al. 2024; Montenegro-Taborda et al. 2023; Contreras-Santos et al. 2024; Pillepich et al. 2018). Conversely, the systematically lower metallicities measured in our

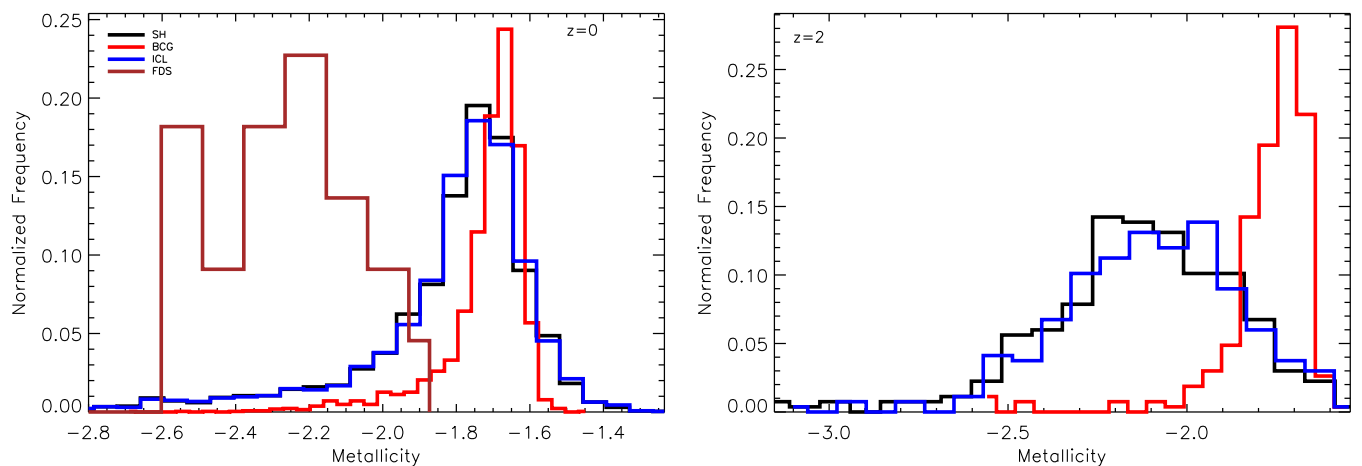


Fig. 8. Similarly to Figure 6, the plots display the metallicity distributions ($\log Z$) for BCGs (red), stellar halos (black), and ICL (blue) at $z = 0$ (left panel) and $z = 2$ (right panel). In both panels, stellar halos and the ICL exhibit broadly comparable distributions, whereas BCGs remain systematically more metal-rich than the other two components, regardless of redshift. The separation is present at all epochs, but appears much more pronounced at $z = 2$. The brown line at $z = 0$ represent the observed distribution in FDS (SHs).

observed samples are consistent with a larger fractional contribution from disrupted dwarfs (e.g. Mouhcine et al. 2005; Harmesen et al. 2017; D’Souza & Bell 2018; Spavone et al. 2017; Ragusa et al. 2021, 2022), plausibly reflecting environmental or selection differences with respect to our central-galaxy sample. In this context, the average metallicity of SHs/ICL is a sensitive diagnostic of the mass spectrum of destroyed progenitors; combining metallicity with α -enhancement and kinematics should further discriminate rapid early enrichment from extended, low-mass accretion histories (Venn et al. 2004; Deason et al. 2016).

4. Conclusions

In this work we have investigated the properties of stellar halos (SHs) of bright central galaxies (BCGs), building on our previous implementation of SH formation in the semianalytic model FEGA25 and extending the analysis to their redshift evolution in terms of scaling relations, colours, and metallicities. Our main findings can be summarized as follows:

1. **Scaling with halo structure.** The SH mass correlates tightly with both the BCG and intracluster light (ICL) masses. While both relations are basically linear, the SH–ICL relation exhibits significantly smaller scatter, as expected from the adopted SH definition, consistent with the direct origin of SHs from ICL stars. Halo concentration emerges as a fundamental driver: less concentrated (typically more massive) halos host more extended transition radii and correspondingly larger SHs. In addition, SHs are more massive in systems with higher ICL formation efficiency, showing that both structural and baryonic processes shape the SH–ICL connection. We note that the residual scatter in these relations reflects variations in halo concentration, ICL assembly histories, and physically motivated stability criteria applied in the model.

2. **Transition radii.** The distribution of R_{trans} predicted by the model peaks around 30–40 kpc nearly independently of redshift, with $\sim 90\%$ of systems below 100 kpc. However, massive halos can reach $R_{\text{trans}} \sim 400$ kpc at $z = 0$. The weak redshift evolution suggests that SH sizes are largely set by halo concentration rather

than epoch, in agreement with recent simulation-based determinations (e.g. Proctor et al. 2024). At the same time, the observational R_{trans} distribution inferred from VEGAS is more narrowly peaked at smaller radii, indicating an offset with respect to the model predictions. This difference reflects the distinct definitions adopted in observations and in the semi-analytic model, as well as sample-selection effects. The comparison should therefore be interpreted in a statistical and qualitative sense, rather than as a direct one-to-one correspondence between individual systems.

3. **Colors.** All three components—BCGs, SHs, and ICL—progressively redden with cosmic time. By $z = 0$, their colour distributions largely overlap, with only a mild offset leaving BCGs redder on average. SHs and ICL are virtually indistinguishable in broad-band colours at all epochs, implying that colours alone are not sufficient to separate these two components observationally. This degeneracy reinforces the idea of a common physical origin and is consistent with the large scatter of observed colour gradients in nearby halos. In the model, colours are derived self-consistently from the star-formation histories of the different stellar components, rather than treated as free parameters.

4. **Metallicities.** At $z = 2$, BCGs are more metal rich than both SHs and ICL by ~ 0.4 dex, but this gap shrinks to ~ 0.1 dex by $z = 0$ as SHs/ICL become progressively more enriched through the stripping of more massive satellites. The convergence of metallicities over time highlights the role of late accretion in building chemically evolved outskirts. FDS observations, however, peak at lower metallicities, suggesting that disrupted dwarf galaxies contribute more strongly to observed halos than in our central-galaxy sample. This points to possible environmental or selection effects and emphasizes the diagnostic power of metallicity gradients for constraining progenitor mass functions.

5. **Overall picture.** SHs appear as transition regions between the stars bound to BCGs and those belonging to the diffuse ICL. We emphasize that this interpretation follows directly from the adopted SH definition, while the trends in mass, structure, and stellar populations discussed in this work reflect genuine phys-

ical dependencies on halo concentration, ICL formation efficiency, and the mass spectrum of accreted satellites. These conclusions support a view in which SHs are not isolated components but rather the inner manifestation of the ICL, dynamically and chemically coupled to the outer galaxy environment. Future wide-field imaging and spectroscopic surveys (e.g. LSST, WEAVE, 4MOST) will be crucial to test these predictions by simultaneously probing structure, metallicity, and kinematics across large samples of halos in diverse environments.

Acknowledgements. The authors thank the anonymous referee for their constructive comments, which have significantly contributed to improving this manuscript. E.C. and S.K.Y. acknowledge support from the Korean National Research Foundation (RS-2025-00514475; RS-2022-NR070872), and E.C. acknowledges support from the Korean National Research Foundation (RS-2023-00241934). M.S. and E.I. acknowledge the support by the Italian Ministry for 1224 Education University and Research (MIUR) grant PRIN 2022 2022383WFT 1225 “SUNRISE”, CUP C53D23000850006 and by VST funds. R.R. acknowledges financial support through grants PRIN-MIUR 2020SKSTHZ and through INAF-WEAVE StePS funds.

References

- Amorisco, N. C. 2017, *MNRAS*, 464, 2882
- Bahé, Y. M., Barnes, D. J., Dalla Vecchia, C., et al. 2017, *MNRAS*, 470, 4186
- Barnes, D. J., Kay, S. T., Bahé, Y. M., et al. 2017, *MNRAS*, 471, 1088
- Beers, T. C., Carollo, D., Ivezić, Ž., et al. 2012, *ApJ*, 746, 34
- Belokurov, V., Erkal, D., Evans, N. W., Koposov, S. E., & Deason, A. J. 2018, *MNRAS*, 478, 611
- Belokurov, V., Sanders, J. L., Fattahi, A., et al. 2020, *MNRAS*, 494, 3880
- Beltrand, C., Monachesi, A., D’Souza, R., et al. 2024, *A&A*, 690, A115
- Bullock, J. S. & Johnston, K. V. 2005, *ApJ*, 635, 931
- Capaccioli, M., Spavone, M., Grado, A., et al. 2015, *A&A*, 581, A10
- Carollo, D., Beers, T. C., Chiba, M., et al. 2010, *ApJ*, 712, 692
- Carollo, D., Beers, T. C., Lee, Y. S., et al. 2007, *Nature*, 450, 1020
- Chabrier, G. 2003, *PASP*, 115, 763
- Child, H. L., Habib, S., Heitmann, K., et al. 2018, *ApJ*, 859, 55
- Contini, E., De Lucia, G., Villalobos, Á., & Borgani, S. 2014, *MNRAS*, 437, 3787
- Contini, E. & Gu, Q. 2020, *ApJ*, 901, 128
- Contini, E., Jeon, S., Rhee, J., Han, S., & Yi, S. K. 2023, *ApJ*, 958, 72
- Contini, E., Rhee, J., Han, S., Jeon, S., & Yi, S. K. 2024a, *AJ*, 167, 7
- Contini, E., Seo, C., Rhee, J., Jeon, S., & Yi, S. K. 2025a, *ApJS*, 281, 2
- Contini, E., Spavone, M., Ragusa, R., Iodice, E., & Yi, S. K. 2024b, *A&A*, 692, L9
- Contini, E., Yi, S. K., & Jeon, S. 2024c, arXiv e-prints, arXiv:2404.01560
- Contini, E., Yi, S. K., Jeon, S., & Rhee, J. 2024d, *ApJS*, 274, 41
- Contini, E., Yi, S. K., & Kang, X. 2018, *MNRAS*, 479, 932
- Contini, E., Yi, S. K., & Kang, X. 2019, *ApJ*, 871, 24
- Contini, E., Yi, S. K., Rhee, J., & Jeon, S. 2025b, *ApJS*, 279, 18
- Contreras-Santos, A., Knebe, A., Cui, W., et al. 2024, *A&A*, 683, A59
- Cooper, A. P., Cole, S., Frenk, C. S., et al. 2010, *MNRAS*, 406, 744
- Cooper, A. P., Martínez-Delgado, D., Helly, J., et al. 2011, *ApJ*, 743, L21
- Cooper, A. P., Parry, O. H., Lowing, B., Cole, S., & Frenk, C. 2015, *MNRAS*, 454, 3185
- Correa, C. A., Wytthe, J. S. B., Schaye, J., & Duffy, A. R. 2015, *MNRAS*, 452, 1217
- Crain, R. A., Schaye, J., Bower, R. G., et al. 2015, *MNRAS*, 450, 1937
- Cui, W., Knebe, A., Yepes, G., et al. 2018, *MNRAS*, 480, 2898
- de Jong, R. S., Agertz, O., Berbel, A. A., et al. 2019, *The Messenger*, 175, 3
- de Vaucouleurs, G. 1959, *Handbuch der Physik*, 53, 275
- Deason, A. J., Belokurov, V., & Evans, N. W. 2013, *ApJ*, 763, 113
- Deason, A. J., Belokurov, V., Koposov, S. E., & Rockosi, C. M. 2014, *ApJ*, 787, 30
- Deason, A. J., Mao, Y.-Y., & Wechsler, R. H. 2016, *ApJ*, 821, 5
- Drinkwater, M. J., Gregg, M. D., & Colless, M. 2001, *ApJ*, 548, L139
- D’Souza, R. & Bell, E. F. 2018, *MNRAS*, 474, 5300
- Duc, P.-A., Cuillandre, J.-C., Karabal, E., et al. 2015, *MNRAS*, 446, 120
- Efron, B. 1979, *The Annals of Statistics*, 7, 1
- Elias, L. M., Sales, L. V., Helmi, A., & Hernquist, L. 2020, *MNRAS*, 495, 29
- Font, A. S., McCarthy, I. G., Crain, R. A., et al. 2011, *MNRAS*, 416, 2802
- Gallart, C., Bernard, E. J., Brook, C. B., et al. 2019, *Nature Astronomy*, 3, 932
- Gendron, V. & Martel, H. 2025, *MNRAS*, 541, 2513
- Gilbert, K. M., Kalirai, J. S., Guhathakurta, P., et al. 2014, *ApJ*, 796, 76
- Gilhuly, C., Merritt, A., Abraham, R., et al. 2022, *ApJ*, 932, 44
- Grand, R. J. J., Gómez, F. A., Marinacci, F., et al. 2017, *MNRAS*, 467, 179
- Guo, Q., White, S., Boylan-Kolchin, M., et al. 2011, *MNRAS*, 413, 101
- Harmsen, B., Monachesi, A., Bell, E. F., et al. 2017, *MNRAS*, 466, 1491
- Helmi, A. 2008, *A&A Rev.*, 15, 145
- Helmi, A. 2020, *ARA&A*, 58, 205
- Helmi, A., Babusiaux, C., Koppelman, H. H., et al. 2018, *Nature*, 563, 85
- Hopkins, P. F., Kereš, D., Oñorbe, J., et al. 2014, *MNRAS*, 445, 581
- Ibata, R. A., Lewis, G. F., McConnachie, A. W., et al. 2014, *ApJ*, 780, 128
- Iodice, E., Capaccioli, M., Grado, A., et al. 2016, *ApJ*, 820, 42
- Iodice, E., Spavone, M., Cantiello, M., et al. 2017, *ApJ*, 851, 75
- Iodice, E., Spavone, M., Capaccioli, M., et al. 2019, *A&A*, 623, A1
- Iodice, E., Spavone, M., Capaccioli, M., et al. 2021, *The Messenger*, 183, 25
- Ivezić, Ž., Kahn, S. M., Tyson, J. A., et al. 2019, *ApJ*, 873, 111
- Jin, S., Trager, S. C., Dalton, G. B., et al. 2024, *MNRAS*, 530, 2688
- Joo, H., Jee, M. J., Kim, J., et al. 2025, *ApJ*, 990, 96
- Kalirai, J. S., Gilbert, K. M., Guhathakurta, P., et al. 2006, *ApJ*, 648, 389
- Krajnović, D., Emsellem, E., den Brok, M., et al. 2018, *MNRAS*, 477, 5327
- Lane, J. M. M., Bovy, J., & Mackereth, J. T. 2022, *MNRAS*, 510, 5119
- Lee, J. & Yi, S. K. 2017, *ApJ*, 836, 161
- Merritt, A., van Dokkum, P., Abraham, R., & Zhang, J. 2016, *ApJ*, 830, 62
- Mihos, J. C., Harding, P., Feldmeier, J. J., et al. 2017, *ApJ*, 834, 16
- Monachesi, A., Gómez, F. A., Grand, R. J. J., et al. 2016, *MNRAS*, 459, L46
- Monachesi, A., Gómez, F. A., Grand, R. J. J., et al. 2019, *MNRAS*, 485, 2589
- Montenegro-Taborada, D., Rodríguez-Gómez, V., Pillepich, A., et al. 2023, *MNRAS*, 521, 800
- Montes, M. & Trujillo, I. 2018, *MNRAS*, 474, 917
- Mouhcine, M., Ferguson, H. C., Rich, R. M., Brown, T. M., & Smith, T. E. 2005, *ApJ*, 633, 810
- Naidu, R. P., Conroy, C., Bonaca, A., et al. 2020, *ApJ*, 901, 48
- Navarro, J. F., Frenk, C. S., & White, S. D. M. 1997, *ApJ*, 490, 493
- Nelson, D., Pillepich, A., Ayromlou, M., et al. 2024, *A&A*, 686, A157
- Nelson, D., Pillepich, A., Springel, V., et al. 2018, *MNRAS*, 475, 624
- Nelson, D., Springel, V., Pillepich, A., et al. 2019, *Computational Astrophysics and Cosmology*, 6, 2
- Oliva-Altamirano, P., Brough, S., Lidman, C., et al. 2014, *MNRAS*, 440, 762
- Pillepich, A., Nelson, D., Hernquist, L., et al. 2018, *MNRAS*, 475, 648
- Pinna, F., Walo-Martín, D., Grand, R. J. J., et al. 2024, *A&A*, 683, A236
- Planck Collaboration, Aghanim, N., Akrami, Y., et al. 2020, *A&A*, 641, A6
- Prada, F., Klypin, A. A., Cuesta, A. J., Betancort-Rijo, J. E., & Primack, J. 2012, *MNRAS*, 423, 3018
- Proctor, K. L., Lagos, C. d. P., Ludlow, A. D., & Robotham, A. S. G. 2024, *MNRAS*, 527, 2624
- Ragusa, R., Iodice, E., Spavone, M., et al. 2023, *A&A*, 670, L20
- Ragusa, R., Mirabile, M., Spavone, M., et al. 2022, *Frontiers in Astronomy and Space Sciences*, 9, 852810
- Ragusa, R., Spavone, M., Iodice, E., et al. 2021, *A&A*, 651, A39
- Sarzi, M., Iodice, E., Coccato, L., et al. 2018, *A&A*, 616, A121
- Schaye, J., Crain, R. A., Bower, R. G., et al. 2015, *MNRAS*, 446, 521
- Seigar, M. S., Graham, A. W., & Jerjen, H. 2007, *MNRAS*, 378, 1575
- Spavone, M., Capaccioli, M., Napolitano, N. R., et al. 2017, *A&A*, 603, A38
- Spavone, M., Iodice, E., Capaccioli, M., et al. 2018, *ApJ*, 864, 149
- Spavone, M., Iodice, E., D’Ago, G., et al. 2022, *A&A*, 663, A135
- Spavone, M., Iodice, E., Lohmann, F. S., et al. 2024, *A&A*, 689, A306
- Spavone, M., Iodice, E., van de Ven, G., et al. 2020, *A&A*, 639, A14
- Spavone, M., Krajnović, D., Emsellem, E., Iodice, E., & den Brok, M. 2021, *A&A*, 649, A161
- Springel, V., Pakmor, R., Zier, O., & Reinecke, M. 2021, *MNRAS*, 506, 2871
- Venhola, A., Peletier, R., Laurikainen, E., et al. 2018, *A&A*, 620, A165
- Venhola, A., Peletier, R., Laurikainen, E., et al. 2017, *A&A*, 608, A142
- Venn, K. A., Irwin, M., Shetrone, M. D., et al. 2004, *AJ*, 128, 1177
- Wright, A. C., Tumlinson, J., Peebles, M. S., et al. 2024, *ApJ*, 970, 70

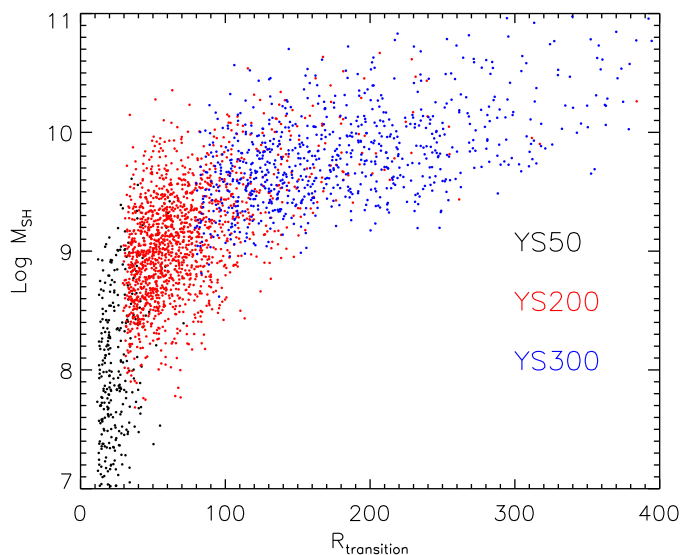


Fig. A.1. Relation between SH mass and transition radius R_{trans} for simulations with different mass resolutions: YS50 (black), YS200 (red), and YS300 (blue). The relations are shown over the stellar-mass ranges covered by each of them. The median trends are consistent within the scatter, with no systematic dependence on numerical resolution, indicating that the SH– R_{trans} relation is robust against resolution effects.

Appendix A: Resolution tests

We assess the impact of numerical resolution on the main scaling relations discussed in this work by comparing results obtained from simulations with different mass resolutions over the stellar-mass ranges where they overlap. In particular, we analyse the relations between SH mass and transition radius, SH mass and BCG stellar mass, and SH mass and ICL mass.

Figure A.1 shows the relation between SH mass and R_{trans} for the different simulations. The median trends and scatter are consistent within the overlapping mass ranges, with no systematic offsets as a function of resolution. Similarly, Figure A.2 compares the SH–BCG and SH–ICL mass relations, which also display fully consistent behaviour across simulations of different resolution.

These tests indicate that the scaling relations presented in the main text are not driven by numerical resolution effects. This result is expected, as the semi-analytic model traces integrated stellar components whose global properties primarily depend on halo assembly histories rather than on the detailed resolution of individual substructures.

We therefore conclude that numerical resolution does not significantly affect the trends discussed in this work. For this reason, additional properties such as colours and metallicities, which are derived from the same integrated stellar populations, are not expected to show a stronger dependence on resolution.

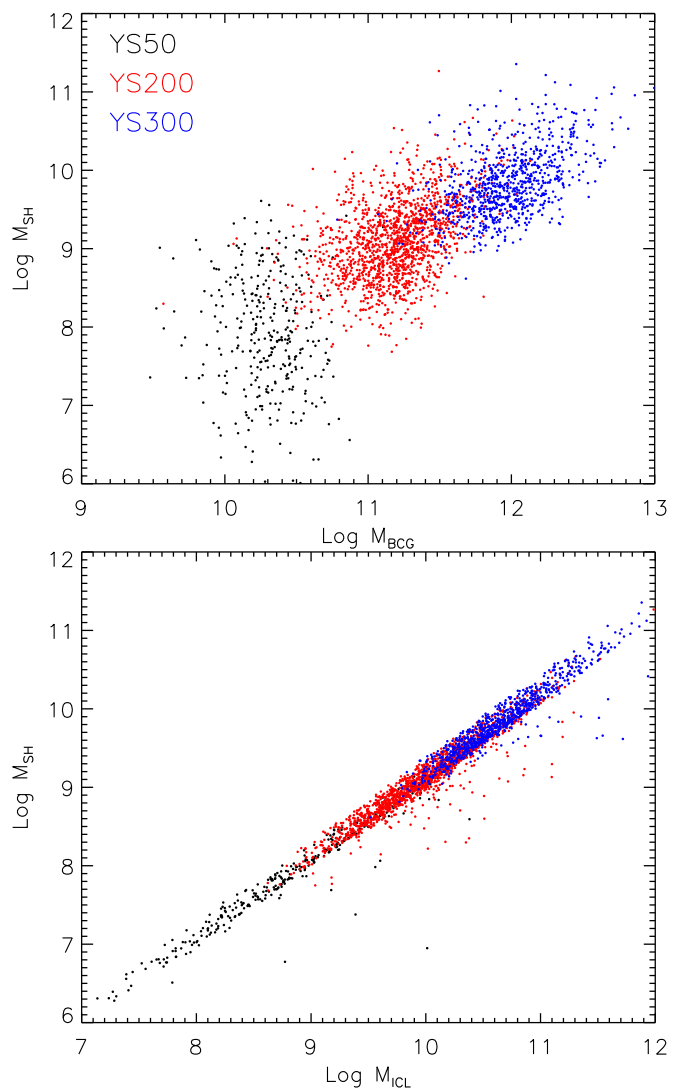


Fig. A.2. Scaling relations between SH mass and BCG stellar mass (upper panel), and SH mass and ICL mass (bottom panel), for simulations with different mass resolutions: YS50 (black), YS200 (red), and YS300 (blue). The agreement between the median relations in the overlapping mass ranges demonstrates that the main scaling relations discussed in the paper are not driven by numerical resolution.